Title

Strong—strong simulations of combined beam—beam and wakefield effects in the Electron—Ion-Collider

Authors
Qiang, J
Blaskiewicz, M

Publication Date
2024-12-01

DOI
10.1016/j.nima.2024.169942

Peer reviewed

Strong-strong simulations of combined beam-beam and wakefield effects in the Electron-Ion-Collider

J. Qiang

Lawrence Berkeley National Laboratory, Berkeley, CA 94720

M. Blaskiewicz

Brookhaven National Laboratory, Upton, NY 11973

Abstract

Collective wakefield and beam-beam effects play an important role in accelerator design and operation. These effects can cause beam instability, emittance growth, and luminosity degradation, and warrant careful study during accelerator design. In this paper, we studied the combined wakefield and beam-beam effects in an Electron Ion Collider design using strong-strong simulations. The simulation results show that the nonlinear beam-beam effects help suppress wakefield driven instability in the nominal working tune regime. In other tune regimes, the coherent beam-beam modes interact with the wakefields and cause a beam instability. The simulation results also show the importance of maintaining nominal crab cavity voltage. If the crab cavity voltage drops significantly the beam can become unstable.

1. INTRODUCTION

The electron-ion collider (EIC) as the next generation collider for high energy nuclear physics research is being actively studied [1]. The EIC consists of two colliding rings, a hadron ring with energy 41-275 GeV and an electron storage ring with energy 5-18 GeV. The nominal design goal is to attain a peak luminosity of $10^{34}\text{cm}^{-2}\text{s}^{-1}$. Such a luminosity requires high electron and proton beam currents. With such high beam currents, coherent instabilities driven by accelerator wakefields become a major concern. Furthermore, the presence of the beam-beam effects from colliding beams further complicates the problem. On one hand, the nonlinear beam-beam interaction of two colliding beams produces tune spread in each beam. This tune spread provides Landau damping to the coherent instability and helps mitigate the instability [2, 3]. On the other hand, the beam-beam interaction of colliding beams also excites coherent modes. These coherent beam-beam modes interact with the accelerator wakefield and cause beam instability [4, 5, 6]. Recently there were reports on the combined short-range wakefield and beam-beam effects in several lepton colliders [7, 8, 9, 10, 11, 12, 13]. In this study, we combine beam-beam, short-range and long-range wakefield effects. The beam-beam effects are modeled as weak-strong, strong-strong using a soft Gaussian approach, and a full strong-strong simulation. Certain instabilities are seen only in the full strong-strong simulation.

2. COMPUTATIONAL MODEL

In the following, we will give a brief overview of the single particle tracking model, wakefield simulation model, and strong-strong beam-beam simulation model.

2.1. Single Particle Tracking Model

Each macroparticle has six coordinates $(x, \tilde{p}_x, y, \tilde{p}_y, \Delta\gamma, \tau)$ [14], where $\tilde{p}_{x,y}$ are normalized transverse momenta, i.e. $\tilde{p}_{x,y} = \frac{p_{x,y}}{p_0}\bar{\beta}_{x,y}$, $\Delta\gamma = \gamma - \gamma_0$ is energy deviation, and τ is the arrival time of the particle with respect to the synchronous phase. The average Twiss beta function value is $\bar{\beta}_{x,y} = c_l/(2\pi\mu_{x,y})$, c_l is the circumference of the ring, p_0 is the total momentum value of the reference particle, and γ_0 is the Lorentz factor of the reference particle of mass m and charge q. The particle horizontal coordinates are updated via a transfer map followed by a single bunch wake kick applied n_u times per turn

$$x = x\cos(\phi/n_u) + \tilde{p}_x \sin(\phi/n_u) \tag{1}$$

$$\tilde{p}_x = -x\sin(\phi/n_u) + \tilde{p}_x \cos(\phi/n_u) \tag{2}$$

where the phase advance per turn is $\phi = \phi_0 + \frac{2\pi\xi}{\beta^2\gamma_0}\Delta\gamma + o_{xx}(x^2 + \tilde{p}_x^2)/(2\bar{\beta}_x) + o_{xy}(y^2 + \tilde{p}_y^2)/(2\bar{\beta}_y)$, $\phi_0 = 2\pi\mu$ is the on-momentum phase advance, ξ is the chromaticity, and o_{xx} and o_{xy} are the magnitudes of amplitude dependent detuning phase factor. The transverse radiation damping and quantum excitation are applied to x once per turn as:

$$x = (1 - \frac{T_0}{T_x})x + \delta x \tag{3}$$

$$\tilde{p}_x = (1 - \frac{T_0}{T_x})\tilde{p}_x + \delta p_x \tag{4}$$

where T_x is the transverse radiation damping time, and δx and δp_x are random variables. The same above equations are applied to the particle vertical coordinates with x replaced by y. The particle longitudinal coordinates are updated n_u times per turn. The update is:

$$\Delta\gamma = \Delta\gamma + \frac{q}{mc^2 n_u}[V(\tau) - V_s] \tag{5}$$

$$\tau = \tau + \frac{T_0\eta}{\beta^2\gamma_0 n_u}\Delta\gamma \tag{6}$$

where $V(\tau)$ is the RF voltage, V_s is the synchronous voltage due to both acceleration and radiation, $\beta = v/c$, T_0 is the revolution period, η is the frequency slip factor. Quantum excitation and radiation damping is updated once per turn.

2.2. Wakefield Simulation Model

Wakes are simulated using standard binning techniques and fast Fourier transforms [14]. The voltage associated with the longitudinal wakefield can be obtained from the following convolution.

$$V_s(t) = -\int_{-\tau_b}^{\tau_b} W_s(\tau) I_b(t-\tau) d\tau \tag{7}$$

where $W_s(\tau)$ is the longitudinal wake potential, and $I_b(t)$ is the instantaneous beam current. The transverse voltage due to the transverse wakefield includes two terms. One is the short range term given by:

$$V_x(x,t) = \int_{-\tau_b}^{\tau_b} [x W_d(\tau) I_b(t-\tau) + W_x(\tau) D_x(t-\tau)] d\tau \tag{8}$$

where $W_d(t)$ will be called the detuning wake [15], $W_x(t)$ is the usual transverse wake potential, and $D_x(t)$ is the instantaneous dipole density. The short range wakes are updated n_u times per turn. This is because most short range wakes are due to a large number of relatively small contributions and are well approximated by a uniformly distributed impedance. If the number of updates per turn is too small, macroparticles can slip past each other longitudinally without interacting, resulting in nonphysical emittance growth.

Transverse multibunch long-range wakefield effects are updated once per turn. We track one bunch, it is assumed that there are M identical, equally spaced bunches interacting with coupled bunch mode number s. On turn n one generates the dipole moment of the tracked bunch at a fixed azimuth (say 0),

$$D_x^0(t,n) = I(t) < x(t) >$$

where $I(t)$ is the instantaneous bunch current and $< x(t) >$ is the centroid of the bunch as it passes. The moment associated with the angular offset is,

$$D_p^0(t,n) = I(t)[\beta_x < x'(t) > +\alpha_x < x(t) >] = I(t) < \tilde{p}_x(t) > .$$

Assuming the coherent tune shift is small, define the dipole moment for all subsequent bunches passing this location on turn n,

$$D_x(t,n) = \sum_{m=0}^{M-1} D_x^0(t - mT_b, n)\cos(m[\psi_\beta - \psi_s])$$
$$+D_p^0(t - mT_b, n)\sin(m[\psi_\beta - \psi_s]). \tag{9}$$

where there are M bunches with period T_b. The betatron phase advance between bunches is $\psi_\beta = 2\pi\mu_x/M$ and the coupled bunch mode phase shift between bunches is $\psi_s = 2\pi s/M$.

The long range wakes $W_x(t) = Re(W(\tau))$ are modeled as a sum of damped oscillators

$$W(\tau) = H(\tau)\sum_{l=1}^{L} W_l \exp(-\alpha_l \tau) \tag{10}$$

where L is the number of wakes and H is the Heaviside function. The transverse voltage is given by

$$V_x(t) = \int_{-\infty}^{t} D_x(t_1) W_x(t - t_1) dt_1. \tag{11}$$

Differentiating equation (11) with respect to t and using equation (10) results in an easily integrable ordinary differential equation for each index l. The integrals for $D_x^0(t,n)$ and $D_p^0(t,n)$ need only be done once. The summation over the rest of the bunches is done directly, since M is always small compared to the number of macroparticles. The wakefields in the vertical direction can be attained by replacing x with y in the above equations.

The wakefield model of the EIC has been steadily improving since 2019 [16]. Wakes for individual components of the Electron Storage Ring have been modeled using CST, GdfidL and ECHO. The vertical long-range wake is dominated by the resistive wall and the horizontal one is dominated by the fundamental mode of the crab cavities. The Hadron Storage Ring broadband impedance can be well characterized by a broadband resonator. The horizontal long-range wake is dominated by the fundamental mode of the crab cavities.

2.3. Strong-Strong Beam-Beam Simulation Model

The beam-beam interaction is simulated using a strong-strong beam-beam code, BeamBeam3D [17, 18]. The BeamBeam3D is a parallel three-dimensional particle-in-cell code to model beam-beam effects in high-energy circular colliders. This code does self-consistent calculation of the electromagnetic forces (beam-beam forces) from two colliding beams (i.e. strong-strong modeling) at the interaction point (IP) each turn. For the head-on collision (with offset), the colliding bunch is longitudinally divided into multiple slices with equal amounts of charge, and each slice collides with all slices of the opposite bunch. The beam-beam forces during the collision are calculated by solving the Poisson equation using a shifted integrated Green function method, which can be computed very efficiently using an FFT-based algorithm on a uniform grid. For the crossing angle collision, two colliding beams are transformed from the lab frame into a boosted Lorentz frame [19, 20], where the beam-beam forces are calculated in the same way as the head-on collision. After the collision the particles are transformed back into the laboratory frame. The BeamBeam3D code can also handle multiple bunches from each beam collision at multiple interaction points (IPs) and includes models for electron lens, conducting wire and crab cavity compensations.

3. Interplay between beam-beam and wakefield effects

The parameters used in this study are from Table 4.15 of the EIC CDR design report [1]. Here, a 275 GeV proton beam collides with a 10 GeV electron beam with a 25 mrad collision angle. The proton beam has a single bunch population of 0.688×10^{11}, and electron beam 1.72×10^{11}. The beam-beam parameters for the proton beam are $(0.012, 0.012)$ and $(0.072, 0.1)$ for the electron beam. The nominal transverse working point tunes are $(29.228, 30.21)$ for the proton beam, and $(51.08, 48.06)$ for the electron beam. The linear chromaticity in the electron storage ring is $(2.5, 2.5)$ and zeros in the hadron storage ring. The long-range and short-range wake functions used in this study are given in Table 1-3 and Fig. 1. The short-range wakefields are applied 10 times per turn, while the long-range wakefields are applied once per turn.

Table 1: Long-range wake in Hadron Storage Ring, all units are MKS

dimension	W_l	α_l
X_1	$1.47\times10^{15}i$	$2.062\times10^5+1.237\times10^9i$
X_2	$0.779\times10^{15}i$	$2.062\times10^5+2.474\times10^9i$
Z_1	1.425×10^{11}-1.620×10^7i	$2.249\times10^5+1.980\times10^9i$

Table 2: Short-range wake in Hadron Storage Ring

dimension	W_l	α_l
X_1	$1.441\times10^{17}i$	$4.712\times10^9+1.825\times10^{10}i$
Y_1	$1.441\times10^{17}i$	$4.712\times10^9+1.825\times10^{10}i$
Z_1	1.001×10^{16}-$2.60\times10^{15}i$	$4.712\times10^9+1.825\times10^{10}i$

Table 3: Long-range wake in Electron Storage Ring

dimension	W_l	α_l
X_1	$4.49\times10^{13}i$	$4.127\times10^6+2.476\times10^9i$
Y_1	$6.0\times10^{12}i$	$2.45\times10^5+2.393\times10^6i$
Z_1	2.282×10^{12}-$2.153\times10^{10}i$	$5.957\times10^7+6.314\times10^9i$

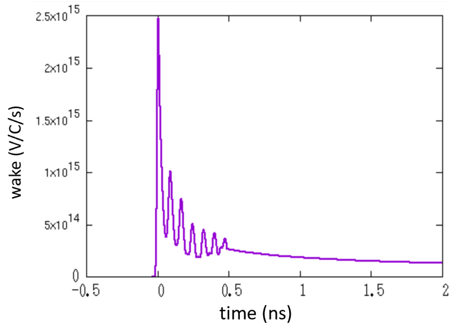

Figure 1: Horizontal short-range wake function in the Electron Storage Ring.

The vertical short-range wake function in the ESR is assumed the same as that in the horizontal dimension.

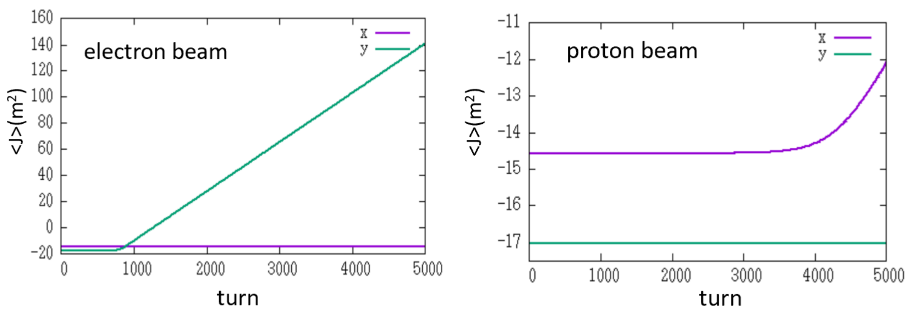

Figure 2: Electron beam natural logarithm average action (top) and proton beam natural logarithm average action (bottom) evolution without beam-beam effects.

In this study, we first check how the electron beam and the proton beam behave with only the wakefield effects. Fig. 2 shows the electron beam logarithm of average action and proton beam average action evolution without the beam-beam effects. Here, the average action is defined as $< x^2 + \tilde{p}_x^2 >$ for the horizontal x action with a similar expression for the vertical y action in this study, and $<>$ denotes average through all macroparticles. It is seen that electron beam vertical average action becomes unstable and grows exponentially after 1000 turns. This instability is caused by the long-range vertical resistive wall wakefield. The proton beam horizontal average action also shows unstable growth. This instability is due to the long-range wakefield of crab cavities in the EIC.

Next, we turn on the beam-beam interaction in the EIC using the strong-strong model of the BeamBeam3D. Fig. 3 shows the electron beam logarithm of average action and proton beam average action evolution with both the wakefield and the beam-beam effects. Both electron beam and proton beam become

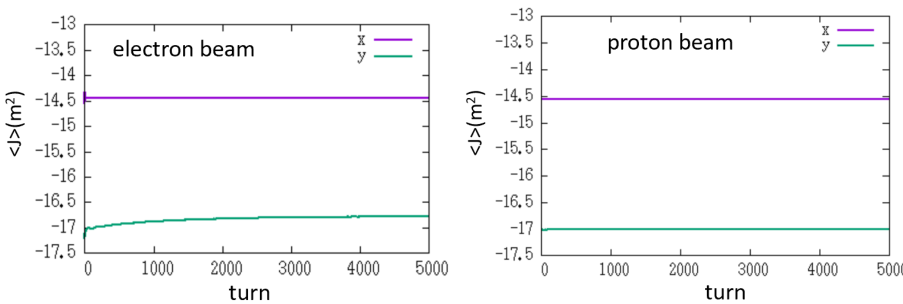

Figure 3: Electron beam natural logarithm average action (top) and proton beam natural logarithm average action (bottom) evolution with both wakefield and beam-beam effects.

stable in the horizontal and vertical dimensions. This is due to the fact that the nonlinear beam-beam interaction induces a tune spread. This tune spread provides Landau damping for the instability and suppresses the instability.

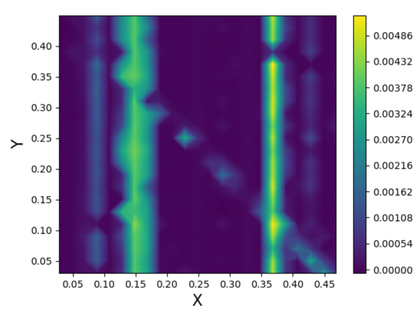

Figure 4: Proton beam horizontal CS_c growth rate versus proton beam transverse tunes.

The instability of colliding beams depends on the tunes of each beam. In this study, we fixed the working tunes of the electron beam, and scanned the working tunes of the proton beam. Here, we define the coherent Courant-Snyder parameter CS_c that is tailored to be a sensitive indicator of instability.

$$CS_c = \frac{\int dt I(t)[\bar{x}^2(t) + \bar{p}^2(t)]}{\int dt I(t)} \tag{12}$$

where $\bar{x}(t)$, and $\bar{p}(t)$ are smoothed average values of x and p as the bunch passes, and $I(t)$ is the smooth current. Figure 4 shows the proton beam horizontal CS_c growth rate as a function of proton beam horizontal and vertical tune. Two strong instability stopbands are seen in this plot. One is around proton beam horizontal 0.15, the other one is around 0.37. These two stopbands are mainly along horizontal tune and independent of vertical tune, which suggests the horizontal instability driven by the crab cavity wakefield. In order to have

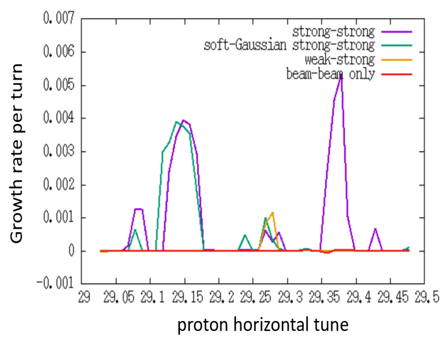

Figure 5: Proton beam horizontal CS_c as a function of proton beam horizontal tune with the nominal CDR electron tune working point $(0.08, 0.06)$ and proton beam vertical tune 0.21. The resonance near $Q_{xp} = 29.37$ appears to be of the form $2Q_{xp} + 2Q_{xe} =$ integer.

better understanding of these stopbands, we fix the proton beam vertical tune, and show in Fig. 5 the instability growth rate as a function of horizontal tune together with the results from the weak-strong beam-beam simulation, the soft-Gaussian simulation and the beam-beam only simulation. Without wakefields (i.e. beam-beam only), there is no strong instability in this figure. With both wakefields and beam-beam effects, we see the above two major stopbands from the self-consistent strong-strong beam-beam simulation. There also exist three minor stopbands along the horizontal tune from the self-consistent strong-strong beam-beam simulation. The weak-strong beam-beam simulation does not show the major instability stopbands except a minor stopband around the $4th$ order resonance. In the weak-strong simulation model, the beam-beam interaction is treated like an external nonlinear field. There is no coherent mode in this model. The nonlinear beam-beam interaction causes individual particle tune spread and results in the Landau damping of the wakefield induced coherent instability. In the strong-strong beam-beam simulation model, the coherent modes can be excited. The coherent mode interacts with the wakefields inside the accelerator and causes coherent instability. The soft-Gaussian strong-strong model does not have a self-consistent beam distribution. We measure the deviation from a Gaussian distribution using excess kurtosis that should be zero for the Gaussian distribution and observe its absolute value significantly greater than zero in the self-consistent strong-strong simulation. We think that this lack of self consistency in the soft-Gaussian model accounts for missing the second major stopband in Fig. 5.

Next, we chose several working points along the proton beam horizontal tune and look into more details of beam centroid evolution. Figure 6 shows the proton and electron beam horizontal center evolution and their power spectra at proton beam tune working point $(0.078, 0.21)$. At this working point, the proton beam horizontal tune is close to the electron beam horizontal tune. It can be seen that both electron beam and the proton beam have the same oscillation frequency and phase, which suggests a sigma type of mode instability. From the spectra, this coherent mode stays out of the continuous incoherent tune spread and will not be damped by incoherent tune spread of the distribution. Figure 7 shows the proton beam horizontal log CS_c evolution at this tune working point with both wakefield and beam-beam effects, with wakefield only and with beam-beam effects only. With both wakefield and beam-beam effects, the CS_c shows

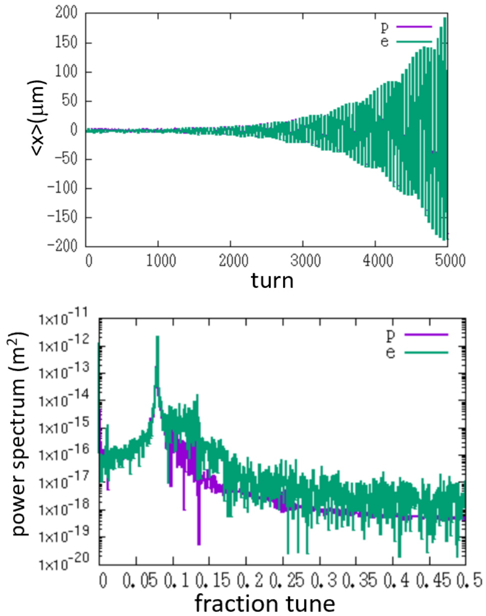

Figure 6: Proton beam and electron beam horizontal centroid evolution (top) and power spectra of the evolution (bottom) with proton beam horizontal tune 0.078. Here, the proton beam centroid overlaps with the electron beam centroid during the evolution.

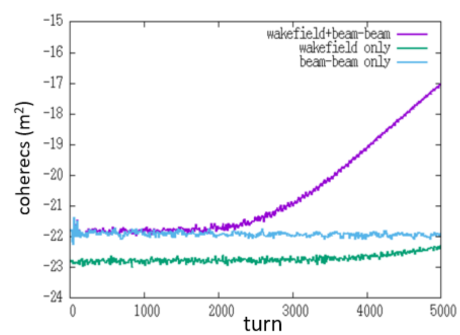

Figure 7: Proton beam horizontal log CS_c evolution with proton beam horizontal tune 0.078 with both wakefield and beam-beam (magenta), wakefield only (green), and beam-beam only (blue).

much larger instability growth rate than the wakefield only case. The unstable coherent beam-beam mode driven by the accelerator wakefields at this tune working point during collision is more dangerous than that without collision.

Figure 8 shows the proton and electron beam horizontal center evolution and

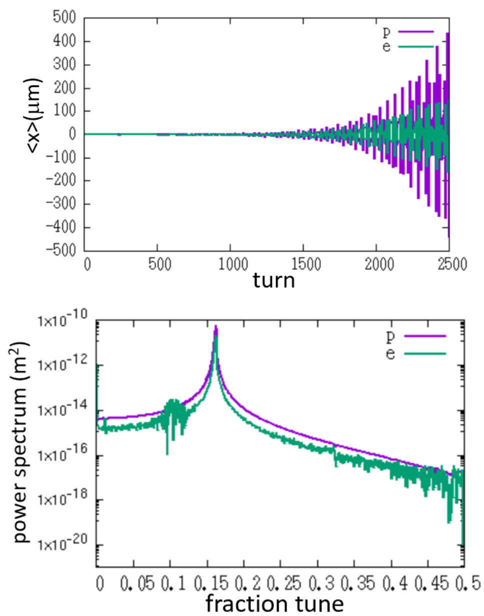

Figure 8: Proton beam and electron beam horizontal centroid evolution (top) and power spectra of the evolution (bottom) with proton beam horizontal tune 0.148.

their power spectra at proton beam tune working point $(0.148, 0.21)$. At this point, the proton beam horizontal tune is close to the electron beam horizontal tune plus the beam-beam parameter. The electron beam oscillation and the proton beam oscillation show 180 degree out of phase, which suggests a pi type of mode instability. From the spectra plot, this coherent pi mode stays out of the continuous incoherent tune spread and is not damped by incoherent tune spread of the distribution. Figure 9 shows the proton beam horizontal log CS_c evolution at this tune working point with both wakefield and beam-beam effects, with wakefield only and with beam-beam effects only. With both wakefield and beam-beam effects, the CS_c shows larger instability growth rate than the wakefield only case. This instability during collision is more dangerous than that without collision.

Figure 10 shows the proton and electron beam horizontal center evolution

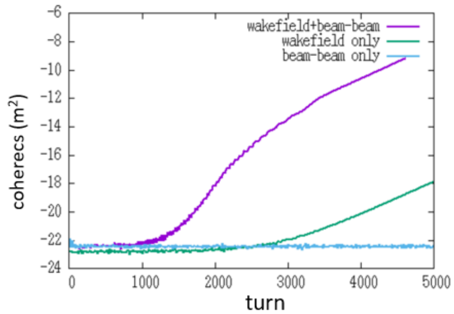

Figure 9: Proton beam horizontal log CS_c evolution with proton beam horizontal tune 0.148 with both wakefield and beam-beam (magenta), wakefield only (green), and beam-beam only (blue).

and their power spectra at proton beam tune working point $(0.368, 0.21)$. At this point, the electron beam and the proton beam interact with each other and fall into the octupole resonance ,i.e. $2Q_{xp}+2Q_{xe} = integer$. The electron beam oscillation and the proton beam oscillation show 180 degree out of phase. From the spectra plot, this coherent mode stays out of the continuous incoherent tune spread and is not damped by incoherent tune spread of the distribution. This mode interacts with the wakefield of the accelerator and becomes unstable. Figure 11 shows the proton beam horizontal log CS_c evolution at this tune working point with both wakefield and beam-beam effects, with wakefield only and with beam-beam effects only. With both wakefield and beam-beam effects, the CS_c shows similar instability growth rate to the wakefield only case. Both instabilities are dangerous before and after collision.

In contrast, Figure 12 shows the proton and electron beam horizontal center evolution and their power spectra at proton beam tune nominal working point $(0.228, 0.21)$. At this working point, the electron beam oscillation and the proton beam oscillation does not show clear phase correlation. From the spectra plot, there is no coherent mode outside the continuous incoherent tune spread. The nonlinear beam-beam interaction generates sufficient tune spread and damps the wakefield driven instability.

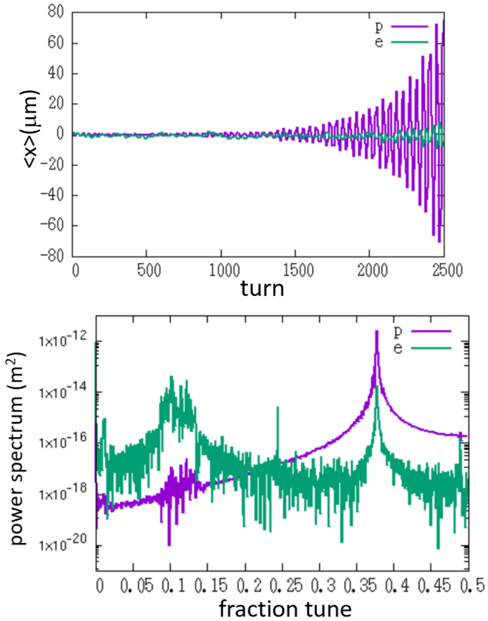

Figure 10: Proton beam and electron beam horizontal centroid evolution (top) and power spectra of the evolution (bottom) with proton beam horizontal tune 0.368.

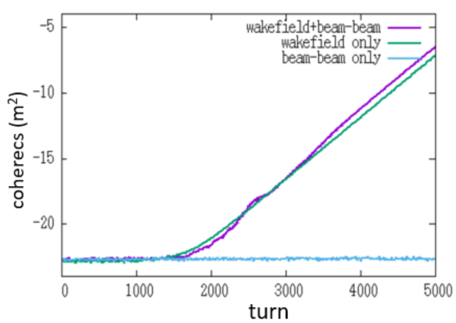

Figure 11: Proton beam horizontal log CS_c evolution with proton beam horizontal tune 0.368 with both wakefield and beam-beam (magenta), wakefield only (green), and beam-beam only (blue).

The coherent beam-beam modes depends on the electron tune working point. Moving the electron beam horizontal tune changes the coherent beam-beam mode frequency and results in a different location of the instability stopband. Figure 13 shows the proton beam horizontal CS_c growth rate as a function of proton beam horizontal tune with electron beam horizontal tune 0.12. Increas-

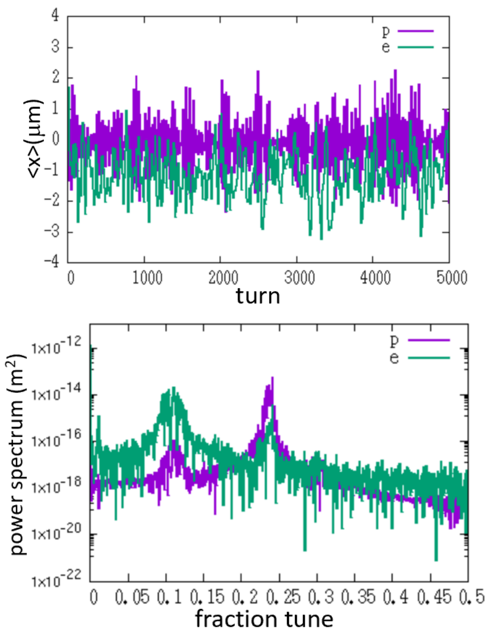

Figure 12: Proton beam and electron beam horizontal centroid evolution (top) and power spectra of the evolution (bottom) with proton beam horizontal tune 0.228.

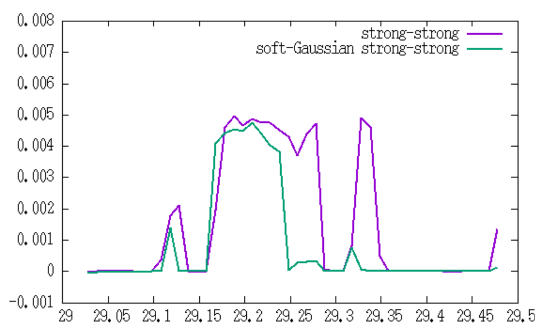

Figure 13: Proton beam horizontal CS_c growth rate as a function of proton beam horizontal tune with a new electron tune working point $(0.12, 0.06)$ and proton beam vertical tune 0.21 from the self-consistent strong-strong model (magenta) and from the soft-Gaussian strong-strong model (green).

ing the electron horizontal tune by 0.04 causes the first two instability stopbands in the proton beam horizontal tune to increase to 0.12 and 0.19 as seen in the above figure. The instability stopband associated with the pi mode becomes wider and merges with 4th order resonance instability stopband. The instability stopband associated with the octupole resonance moves down by about 0.04 to 0.33. The soft-Gaussian model shows similar instability stopbands to the self-consistent model for the sigma mode and pi mode instability. However, the soft-Gaussian model gives much smaller instability stopband around 0.32 than the self-consistent strong-strong model. We suspect this is due to the fact that the soft-Gaussian model assumes a transverse Gaussian distribution and has a different octupole component from the self-consistent strong-strong model.

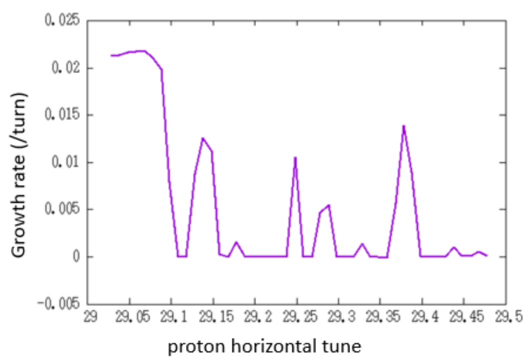

Figure 14: Proton beam horizontal CS_c growth rate as a function of proton beam horizontal tune with proton beam mode 25 and nominal electron tune working point $(0.08, 0.06)$ and proton beam vertical tune 0.21.

Figure 14 shows proton beam horizontal CS_c growth rate as a function of proton beam horizontal tune with a proton beam mode 25 and the nominal electron beam tune working point and the proton beam vertical tune working point. The treatment of the coupled bunch mode 's' is given in the Eq. 9 of this paper. It is seen that there exits similar instability stopbands to the mode 29 in the above simulations except that the growth rate in these stopbands is significantly greater than that with the mode 29.

4. Effects of Crab Cavity Voltage on Beam Instability

In order to compensate the geometric luminosity loss from crossing angle collision, in the EIC, two group of crab cavities located at 90 degree phase advance away from the interaction point (IP) on both sides of the IP are used to correct the collision angle so that two beams collide head-on at the IP. The voltage of the crab cavity is set as [21]:

$$V_{nominal} = \frac{Ec\tan(\theta_c/2)}{q\omega\sqrt{\beta^*\beta_{cc}}} \tag{13}$$

This nominal voltage will fully compensate crossing angle at the IP. In practical operation, if there is a RF power loss or other accident, the crab cavity might not be able to operate with the nominal voltage. Fig. 15 shows the electron beam average vertical action and the proton beam average horizontal action evolution with several crab cavity voltages. Without RF power inside the crab

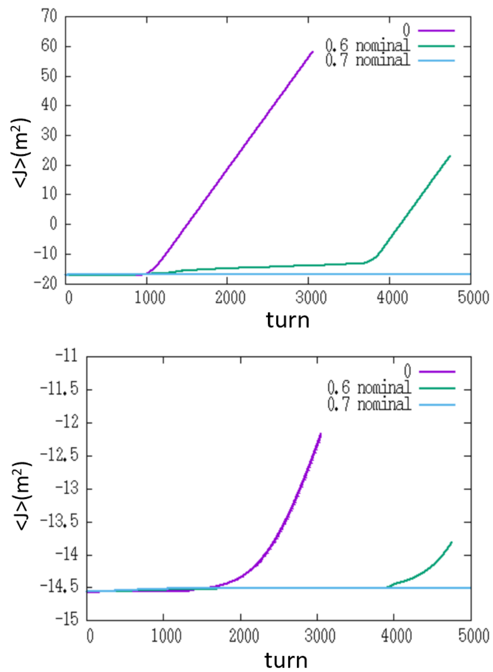

Figure 15: Electron beam natural logarithm vertical average action (top) and proton beam natural logarithm horizontal average action (bottom) evolution with 0×, 0.6×, and 0.7× nominal voltages.

cavity, strong instability is seen in both electron beam and the proton beam.

Even with 0.6× nominal voltage, both beams still become unstable until 0.7× nominal voltage is restored inside the cavity. Losing voltage inside the crab cavity results in less correction of crossing angle and weaker beam-beam interaction. This causes the shrink of tune spread and the loss of Landau damping to the instability.

In order to mitigate the instability due to the loss of RF power inside the crab cavity, we tested the effects of larger chromaticity on beam instability. Figure 16 shows proton beam and electron beam horizontal centroid evolution with a chromaticity of 60, 80, and 100. Larger chromaticity results in smaller growth rate of the instability. It appears that in order to completely suppress the instability under RF failure of the crab cavity, one has to set the chromaticity beyond 100, a value that might not be practically attainable.

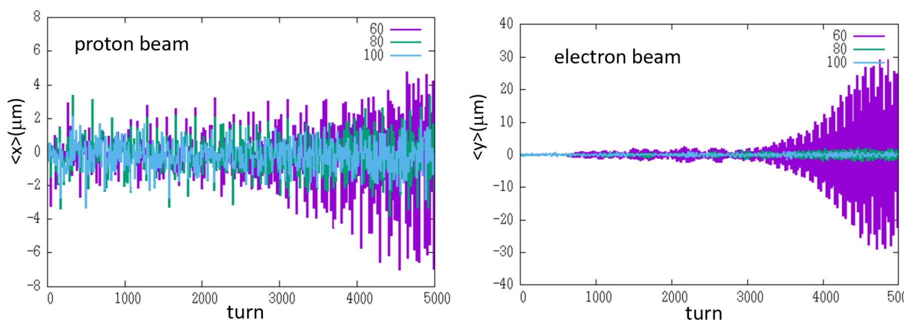

Figure 16: Proton beam horizontal centroid (top) and electron beam vertical centroid (bottom) evolution with 0 crab cavity voltage and chromaticity 60, 80, and 100.

Another option to mitigate the instability is to use octupole magnets to generate large amplitude dependent tune spread. Figure 17 shows proton beam and electron beam horizontal centroid evolution with an amplitude dependent tune magnitude of 160, 640, and 25600. With a nominal horizontal emittance of 20 nm these correspond to average tune shifts of $\Delta\mu = 5.1 \times 10^{-7}, 2.0 \times 10^{-6}, 8.2 \times 10^{-5}$, respectively. Even with a factor of 25600 amplitude dependent tune spread, two beams still become unstable with a total failure of crab cavity.

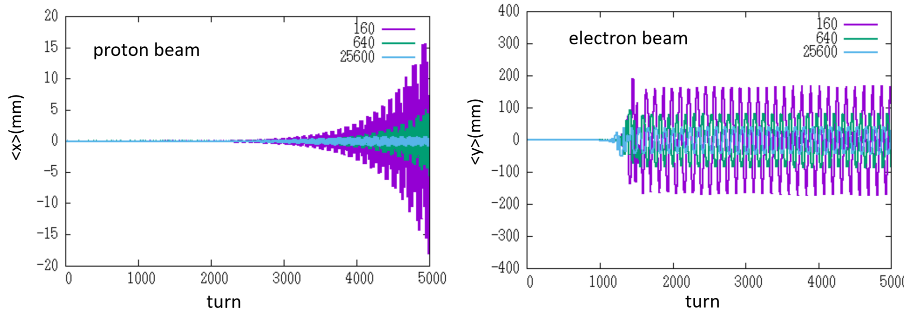

Figure 17: Proton beam horizontal centroid (top) and electron beam vertical centroid (bottom) evolution with amplitude dependent tune 160, 640, and 25600.

We also check whether this instability can be avoided by lowering the bunch intensity under the RF failure inside the crab cavity. Figure 18 shows the proton beam and electron beam horizontal centroid evolution with $0.01\times$, $0.005\times$, and $0.001\times$ nominal bunch population. It appears that the beam bunch intensity has to be lower than $0.001\times$ in order for both beams to become stable.

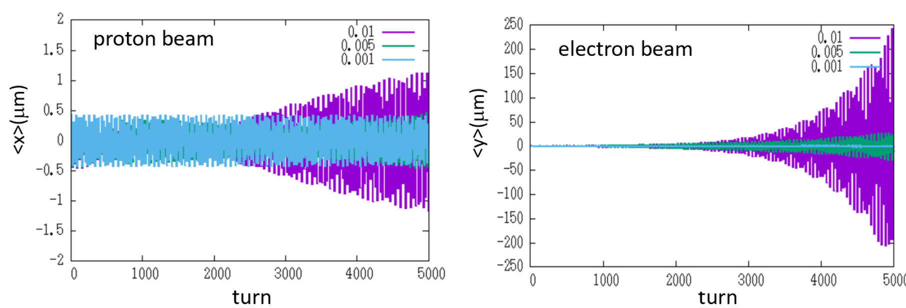

Figure 18: Proton beam horizontal centroid (top) and electron beam vertical centroid (bottom) evolution with $0.01\times$, $0.005\times$, and $0.001\times$ nominal bunch intensity.

5. Impedance Budget with Beam-Beam Effects

The wakefields used in this study are based on the nominal EIC design. It would be interesting to know how far one can deviate from these designed values. The long-range crab cavity wakefield is the dominant factor causing proton beam instability. This wakefield is characterized by a frequency, a damping rate, and

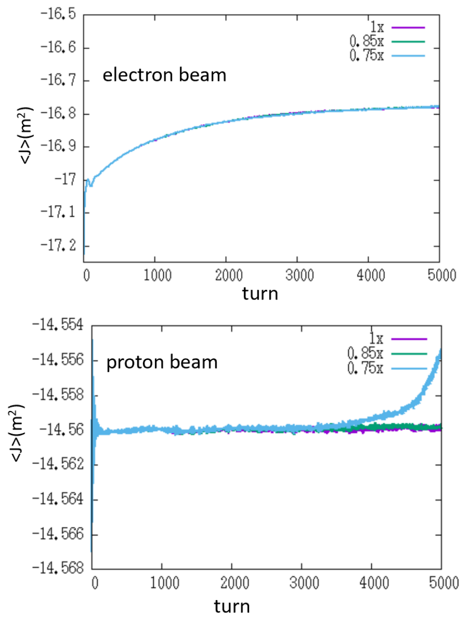

Figure 19: Electron beam natural logarithm vertical average action (top) and proton beam natural logarithm horizontal average action (bottom) evolution with 1×, 0.85×, and 0.75× nominal damping rate.

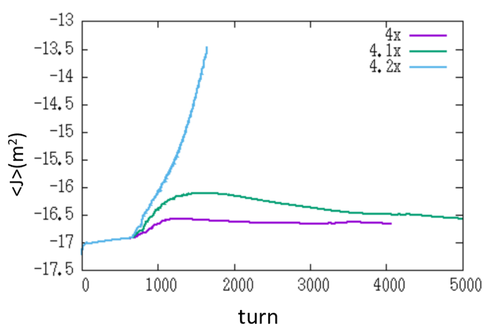

Figure 20: Electron beam natural logarithm vertical average action evolution with 4×, 4.1×, and 4.2× nominal electron ring resistive wall wakefield amplitude.

an amplitude. Fig. 19 shows the electron beam vertical average action and proton beam horizon average action evolution with the nominal damping rate, 0.85× the nominal damping rate, and 0.75× damping rate. A 25% reduction in damping rate causes the proton beam to become unstable. There is not a lot of margin of the damping rate in the crab cavity design with only direct RF feedback.

The long-range vertical resistive wall wakefield contributes to the electron beam instability. Fig. 20 shows the electron beam vertical average action and proton beam horizon average action evolution with 4× the nominal wakefield amplitude, 4.1×, and 4.2× the nominal amplitude. The electron beam becomes unstable with 4.2× nominal amplitude. This gives a large margin of resistive wall impedance in the electron storage ring for such an instability.

6. Conclusions

In this paper, we studied the combined beam-beam and wakefield effects in the Electron Ion Collider using self-consistent strong-strong simulations. Our simulation results show that the interplay between the beam-beam effects and the wakefields effects shows complicated tune dependency. For the nominal design working tunes, the nonlinear beam-beam effects help stabilize both beams against the wakefield driven instability. For some other tunes, the coherent beam-beam modes interact with the wakefields and cause beam instability. These instability stopbands limit the adjustable working tune range during accelerator operation. We also did simulations with only the short-range wakefields and the strong-strong beam-beam interactions and didn't observe these instability stopbands.

Moreover, we studied the crab cavity voltage effects on the beam stability for the nominal tunes. In case of completely losing of RF power inside the crab cavities, both beams would become unstable. Under this situation, it is difficult to restore the stability even with large chromaticity from sextupole or amplitude dependent tune spread from octupole. If the total crab cavity voltage can be maintained more than 70%, the beam can still stay stable, with the damping from the nonlinear beam-beam effects.

We also investigated the margin of the impedance in the current EIC design. It seems that there is not much margin in the crab cavity impedance damping rate (15%) before the proton beam becomes unstable. There is larger margin in the electron ring resistive wall impedance, which can be a factor of 4 of the current level.

In this study, we employed fully self-consistent beam-beam simulations and none self-consistent weak-strong and soft Gaussian strong-strong simulations. Our simulation results show significant discrepancies in the instability tune stopbands along the proton beam horizontal tune space. The self-consistent simulations might be needed in some applications like EIC in order to accurately identify the safe working point regime in the tune space.

ACKNOWLEDGEMENTS

The work of J. Qiang was supported by the U.S. Department of Energy under Contract No. DE-AC02-05CH11231, and used computer resources at the National Energy Research Scientific Computing Center (NERSC). The work of M. Blaskiewicz was supported by Brookhaven Science Associates, LLC under Contract No. DESC0012704 with the U.S. Department of Energy.

References

[1] J. Beebe-Wang ed., "Electron-Ion-Collider at Brookhaven National Laboratory Conceptual Design Report,", 2021, `https://www.bnl.gov/EC/files/EIC_CDR_Final.pdf`.

[2] M.G. Minty *et.al.*, "Recent beam-beam experience with multiple high current bunches in PEP-II", SLAC-PUB-8202. (2000). `doi:10.2172/753279`

[3] R. Li and M. Blaskiewicz, “Impact of choherent beam-beam interaction on the landau dampling of the transverse coupled-bunch instability”, in *Proc. IPAC2021*, Campinas, SP. Brail, p. 2062.

[4] E. A. Perevedentsev and A. A. Valishev, Phys. Rev. ST Accel. Beams 4, 024403 (2001).

[5] E. G. Stern, J. F. Amundson, P. G. Spentzouris, and A. A. Valishev, Phys. Rev. ST Accel. Beams 13, 024401 (2010).

[6] S. White, X. Buffat, N. Mounet, and T. Pieloni, Phys. Rev. ST Accel. Beams, vol 17, p. 041002, 2014. doi:10.1103/PhysRevSTAB.17.041002

[7] Y. Zhang, N. Wang, C. Lin, D. Wang, C. Yu, K. Ohmi, and M. Zobov, Phys. Rev. Accel. Beams 23, 104402 (2020).

[8] D. Leshenok, S. Nikitin,Y. Zhang, and M. Zobov, Phys. Rev. Accel. Beams 23, 101003 (2020).

[9] M. Migliorati, E. Carideo, D. De Arcangelis, Y. Zhang, and M. Zobov, Eur. Phys. J. Plus 136, 1190 (2021).

[10] C. Lin, K. Ohmi, and Y. Zhang, Phys. Rev. Accel. Beams 25, 011001 (2022).

[11] K. Ohmi, Y. Zhang, and C. Lin, Phys. Rev. Accel. Beams 26, 111001 (2023).

[12] D. Zhou, K. Ohmi, Y. Funakoshi, Y. Ohnishi, and Y. Zhang, Phys. Rev. Accel. Beams 26, 071001 (2023).

[13] Y. Zhang, N. Wang, K. Ohmi, D. Zhou, T. Ishibashi, and C. Lin, Phys. Rev. Accel. Beams 26, 064401 (2023).

[14] M. Blaskiewicz, “The TRANFT User’s Manual”, BNL-77074-2006-IR, 2006.

[15] R.L. Gluckstern, J. van Zeijts, B. Zotter, Phys. Rev. E 47, p.656 (1993).

[16] A. Blednykh *et.al.* "An Overview of the Collective Effects and Impedance Calculation for the EIC", THPAB238 in *proc. of IPAC 2021*, Campinas, SP. Brail, p. 4266.

[17] J. Qiang, M. Furman, and R. Ryne, Phys. Rev. ST Accel. Beams, vol 5, 104402 (2002).

[18] J. Qiang, M. Furman, and R. Ryne, J. Comp. Phys. vol. 198, 278 (2004).

[19] K. Hirata, *Phys. Rev. Lett.*, vol. 74, no. 12, p. 2228, 1995. `doi:10.1103/PhysRevLett.74.2228`

[20] L.H.A. Leunissen, F. Schmidt, G. Ripken, *Phys. Rev. ST Accel. Beams*, vol. 3, p. 124002, 2000. `doi:10.1103/PhysRevSTAB.3.124002`

[21] J. Qiang, S. Paret, A. Ratti, J. Barranco, T. Pieloni, G. Arduini, X. Buffat, Y. Papaphilippou, *Nuclear Instruments & Methods in Physics Research A* vol. 900, pp. 53-59, 2018. `do:10.1016/j.nima.2018.05.055`

Appendix A. Semi analytic model

In this section we present a semi analytic model based on the Vlasov equation. All calculations are done in the smooth approximation where the forces are distributed around the accelerator. The general scheme is to calculate the beam response to an external drive. We then use a generalized version of the Nyquist stability condition to test for stability. Take azimuth, θ as the timelike variable and take two beams with distribution functions $F_i(\psi_x, J_x, \psi_y, J_y; \theta)$ for $i = 1, 2$. The Vlasov equations are

$$\frac{\partial F_i}{\partial \theta} + \{F_i, H_i\} = 0 \tag{A.1}$$

where

$$\{A,B\} = \frac{\partial A}{\partial \psi_x}\frac{\partial B}{\partial J_x} - \frac{\partial A}{\partial J_x}\frac{\partial B}{\partial \psi_x} + \frac{\partial A}{\partial \psi_y}\frac{\partial B}{\partial J_y} - \frac{\partial A}{\partial J_y}\frac{\partial B}{\partial \psi_y}$$

is the Poisson bracket. We consider linear betatron oscillations and the beam beam force. For the beam beam force we take a round Gaussian beam. Using standard techniques one may show that the potential in Cartesian coordinates is

$$U(x,y) = 2\sigma^2 \int\limits_0^{1/2\sigma^2} \frac{d\lambda}{\lambda}\left(1 - \exp(-\lambda[x^2+y^2])\right) = x^2 + y^2 + O(r^4). \qquad \text{(A.2)}$$

Henceforth we set $\sigma = 1$ and relate Cartesian and action angle variables via $x = \sqrt{2J_x}\sin\psi_x, \ldots$ For beam 1 we take $H = H_{10} + H_{11}$ with

$$H_{10} = Q_{1x}J_x + Q_{1y}J_y + \xi_1 \left\langle U(\sqrt{2J_x}\sin\psi_x, \sqrt{2J_y}\sin\psi_y\right\rangle_{\psi_x,\psi_y}$$

where the angular brackets denote averaging over the angular variables and H_{10} is purely a function of the actions. The beam-beam parameter is given by ξ_1.

In the perturbing Hamiltonian we include both the beam-beam force and coherent forces associated with impedances with the parameters α_1 and β_1. Without phase averaging it is given by

$$H_{11} = x[2\beta_1\bar{x}_1(\theta) - 2\alpha_1\bar{p}_1(\theta)] - \bar{x}_2(\theta)\xi_1\frac{\partial U}{\partial x} + xD_1(\theta) \qquad \text{(A.3)}$$

where $p = \sqrt{2J_x}\cos\psi_x$, $D_1(\theta)$ is an external drive and

$$\bar{x}_1(\theta) = \int dJ_x d\psi_x dJ_y d\psi_y \sqrt{2J_x}\sin\psi_x F_1(\psi_x, J_x, \psi_y, J_y; \theta)$$

with similar definitions for $\bar{p}_1(\theta), \bar{x}_2(\theta)$. The horizontal coherent tune of beam 1 is $Q_{cohere} \approx Q_{1x} + \beta_1 + i\alpha_1$ in the absence of the beam-beam force. Positive

α corresponds to growth.

Phase averaging the force in (A.3) yields

$$\frac{\partial U}{\partial x} \to \sqrt{2J_x}\sin\psi_x U_c(J_x, J_y), \qquad U_c(J_x, J_y) = \sqrt{\frac{2}{J_x}}\left\langle \sin\psi_y \frac{\partial U}{\partial x}\right\rangle_{\psi_x,\psi_y}$$

For both beams we take the coherent force to be in the x direction. Take the external drive to be $D(\theta) = \hat{D}\exp(-i[\nu + i\epsilon]\theta)$. Then

$$F_1 = F_{10}(J_x, J_y) + \hat{F}_{11}(J_x, \psi_x, J_y)\exp(-i[\nu + i\epsilon]\theta),$$

and the Vlasov equation becomes

$$-i(\nu + i\epsilon)\hat{F}_{11} + \frac{\partial H_{10}}{\partial J_x}\frac{\partial \hat{F}_{11}}{\partial \psi_x} = \frac{\partial \hat{H}_{11}}{\partial \psi_x}\frac{\partial F_{10}}{\partial J_x}. \tag{A.4}$$

Since $\hat{H}_{11} = \tilde{H}_1(J_x, J_y)\sin\psi_x$ we can take $\hat{F}_{11} = \hat{F}_{1c}\cos\psi_x + \hat{F}_{1s}\sin\psi_x$. Inserting in the Vlasov equation and solving yields

$$F_{1s} = \frac{\partial H_{10}}{\partial J_x}\frac{\tilde{H}_1\dfrac{\partial F_{10}}{\partial J_x}}{\left(\dfrac{\partial H_{10}}{\partial J_x}\right)^2 - (\nu + i\epsilon)^2} \tag{A.5}$$

and

$$F_{1c} = -i(\nu + i\epsilon)\frac{\tilde{H}_1\dfrac{\partial F_{10}}{\partial J_x}}{\left(\dfrac{\partial H_{10}}{\partial J_x}\right)^2 - (\nu + i\epsilon)^2}. \tag{A.6}$$

Now we have

$$\hat{\hat{x}}_1 = \int \sqrt{J_x/2}F_{1s}dJ_x dJ_y, \qquad \hat{\hat{p}}_1 = \int \sqrt{J_x/2}F_{1c}dJ_x dJ_y$$

So the moment equations for beam 1 close as

$$\hat{\hat{x}}_1 - \int dJ_x dJ_y \frac{J_x \dfrac{\partial F_{10}}{\partial J_x}\dfrac{\partial H_{10}}{\partial J_x}}{\left(\dfrac{\partial H_{10}}{\partial J_x}\right)^2 - (\nu + i\epsilon)^2} \left\{2\beta_1 \hat{\hat{x}}_1 - 2\alpha_1 \hat{\hat{p}}_1 - \xi_1 \hat{\hat{x}}_2 U_c(J_x, J_y) - \hat{D}_1\right\} = 0$$

and

$$\hat{\hat{p}}_1 - \int dJ_x dJ_y \frac{J_x \dfrac{\partial F_{10}}{\partial J_x}(\epsilon - i\nu)}{\left(\dfrac{\partial H_{10}}{\partial J_x}\right)^2 - (\nu + i\epsilon)^2} \left\{2\beta_1 \hat{\hat{x}}_1 - 2\alpha_1 \hat{\hat{p}}_1 - \xi_1 \hat{\hat{x}}_2 U_c(J_x, J_y) - \hat{D}_1\right\} = 0$$

For beam 2 one switches the first index from 1 to 2 and vice-versa. This gives four equations which can be written in matrix form

$$q_j - \sum_{k=1}^{4} M_{jk}(\nu + i\epsilon) q_k = d_j \tag{A.7}$$

where the $q_1 = \hat{\hat{x}}_1$ etc. and all the interesting physics is in the matrix elements $M_{jk}(\nu + i\epsilon)$. To study stability, plot $Det[\mathbf{1} - \mathbf{M}(\nu + i\epsilon)]$ on the complex plane. If this curve does not encircle the origin the system has an inverse and the beam is stable. If it does encircle the origin increase ϵ until it passes through the origin. That value of ϵ is the imaginary part of the coherent tune for the chosen set of parameters. For a Gaussian kick in equation (A.2) one finds

$$U_c = 2\frac{\partial < U >}{\partial J_x} = 4\int_0^{1/2} d\lambda \exp(-\lambda(J_x + J_y)) I_0(\lambda J_y)\left[I_0(\lambda J_x) - I_1(\lambda J_x)\right].$$

Inserting this into the M_{jk} and finding growth rates yields result similar to the soft Gaussian curve in Figure 5, although only the large single bump is observed. That is to say, the soft Gaussian model significantly underestimates the unstable region and a full strong strong model with all the internal modes is needed for a reliable prediction.